



CHORUS

This is the accepted manuscript made available via CHORUS. The article has been published as:

Lattice softening in body-centered-cubic lithium-magnesium alloys

I. S. Winter, T. Tsuru, and D. C. Chrzan

Phys. Rev. Materials **1**, 033606 — Published 11 August 2017

DOI: [10.1103/PhysRevMaterials.1.033606](https://doi.org/10.1103/PhysRevMaterials.1.033606)

Lattice softening in body-centered-cubic lithium-magnesium alloys

I. S. Winter,^{1,2,*} T. Tsuru,³ and D. C. Chrzan^{1,4,†}

¹*Department of Materials Science and Engineering,
University of California, Berkeley, California 94720, USA*

²*Energy Technologies Area Division,
Lawrence Berkeley National Laboratory, Berkeley, California, 94720, USA*

³*Nuclear Science and Engineering Center, Japan Atomic Energy Agency,
2-4 Shirakata, Tokai-mura, Ibaraki, Japan*

⁴*Materials Sciences Division, Lawrence Berkeley
National Laboratory, Berkeley, California, 94720, USA*

Abstract

A first-principles investigation of the influence of lattice softening on lithium-magnesium alloys near the body-centered-cubic (BCC)/hexagonal close-packed (HCP) transition composition is presented. Results show that lithium-magnesium alloys display a softening of the shear modulus, $C_{11} - C_{12}$, and an acoustic phonon branch between the Γ and N high symmetry points, as the composition approaches the stability limit for the BCC phase. This softening is accompanied by an increase in the size of the dislocation core region. Ideal tensile strength calculations predict that ordered phases of lithium-magnesium alloys are intrinsically brittle. Methods to make the alloys more ductile are discussed, and the propensity for these alloys to display Gum-Metal-like behavior is assessed.

I. INTRODUCTION

The discovery of Gum Metal,¹ a body-centered-cubic (BCC) Ti-Nb based super-elastic, high-strength alloy has produced a great deal of interest within the metallurgical community. These alloys display numerous anomalous and attractive features, but it is their yield near their predicted ideal shear strength (ISS) that has generated the most controversy. In the original paper on this alloy the observation of giant faults as well as a yield stress of approximately 1.1 GPa (on the order of ISS) led to speculation that Gum Metal was a bulk material with deformation determined by its ISS. It was suggested that metals having an average valence electron number of 4.24 electrons/atom, a bond order of approximately 2.87 as well as a d-electron orbital energy level of 2.45 eV should form Gum Metal after undergoing severe plastic deformation. Further studies have not been able to reach a consensus regarding the primary deformation mechanisms of Gum Metal. Evidence for dislocation mediated plasticity has been observed in several cases,^{2,3} while other studies have proposed the novel deformation behavior to be due to a martensitic transformation between the BCC phase, β , and a face centered orthorhombic (FCO) phase, α'' , of Gum Metal.⁴⁻⁶

A theory has been developed that explains the observed deformation at near ISS as the result of the shear modulus $C' = (C_{11} - C_{12})/2$ approaching zero as the composition is driven to the BCC / hexagonal close-packed (HCP) transition.⁷ A particular form of elastic anisotropy increases as this transition composition is neared. This has three major implications related to the deformation behavior of the material. First, the shear modulus along the $\langle 111 \rangle$ direction, $G_{\langle 111 \rangle}$, (typically the softest direction of shear in a BCC material) is proportional to C' . Since ISS is proportional to this shear modulus, the predicted ISS decreases as the transition composition is approached. Second, the particular elastic anisotropy is linked to how easily a dislocation can be pinned. As the BCC/HCP transition is neared the density of pinning points needed to pin the dislocation at applied stresses equal to ISS decreases markedly. This pinning of dislocations at ISS is a necessary condition for a bulk material to deform at ISS. Third, the particular elastic anisotropy has been linked to the spreading of dislocation cores.⁸ The spreading of dislocation cores generally reduces the mobility of the dislocations, and can have a marked influence on plasticity.

Investigations of the phonon dispersion give further insight into a bulk material's tendency to deform via a shear instability. For BCC metals, the reduction in C' and thus the decrease

in ISS is associated with a softening of the acoustic phonons along $\Gamma \rightarrow N$.⁹ The softening of these phonons is also associated with the Burgers path¹⁰ between the BCC and HCP phase. It has been argued that the softening of these phonons can result in shear faults similar to those seen in experiment.^{1,9}

It is posited here that a material, that (1) displays a high value of the proper elastic anisotropy parameter, $K/G_{(111)}$ (K being the modulus governing dislocation line tension), (2) exhibits the softening of phonons along $\Gamma \rightarrow N$, and (3) is intrinsically ductile,⁷ is a candidate for the formation of Gum-Metal-like behavior. If this is true, one should be able to screen for new Gum Metal alloys by computing the elastic constants and ideal strength of candidates.¹¹

Here, Li-Mg alloys are suggested as an interesting candidate for Gum-Metal-like behavior. The BCC phase is elastically unstable at ambient temperature and pressure in pure Mg.¹² In addition, the binary phase diagram shows no intermetallics and a large region of BCC stability.¹³ Previous studies have demonstrated that after severe plastic deformation, either by equal-channel angular pressing^{14,15} or high pressure torsion,¹⁶ on a two phase (BCC and HCP) 8 wt. % Li alloy super-plasticity is achieved at a relatively low temperature. high pressure torsion was shown to induced super-plasticity at 323 K ($0.37T_m$), with the strain rate sensitivity estimated to be 0.3, lower than 0.5, the value typically associated with plastic deformation via grain boundary sliding. This suggests that other mechanisms for plastic deformation could be operative. Interestingly, the application of high pressure torsion on a Fe-Ni-Co-Ti alloy existing near a BCC to face-centered cubic (FCC) instability results in Gum-Metal-like properties, such as an elastic limit of approximately 2% and a yield strength of 2.3 GPa.¹⁷

First-principles investigations of a range of Li-Mg alloys have shown these alloys to have an especially low value of C' .^{18,19} Using the ratio of the bulk modulus to the isotropic shear modulus (B/G , also known as the Pugh ratio) as a measure of ductility²⁰ ordered compounds of composition between 40 and 80 at. % Mg were assessed to be brittle despite their low value for C' . However, Mn, Fe, Co, Ni, Cl and Cu were shown to increase the assessed ductility of the ordered 50 at. % B2 structure²¹ according to the Pugh ratio. This effect is important, as it is unlikely that a brittle material will deform at ISS.⁷

In this paper Li-Mg alloys are evaluated as Gum Metal candidates via three criteria: intrinsic ductility, high elastic anisotropy, and softening of the acoustic phonons along $\Gamma \rightarrow N$.

In addition, an approach is described to model dislocation cores of random solid solutions from first principles, and applied to a Li-Mg alloy near the BCC/HCP transition to better assess the possible connection between this system and Gum Metal. Here, we show through dislocation core radius and elastic anisotropy calculations that Li-Mg alloys display remarkable similarities to Gum Metal, including the apparent formation of nanodisturbances (nanoscale regions of local shear²²) due to the interaction of widely spread cores of $\langle 111 \rangle$ type screw dislocations. However, investigation of the ideal tensile strength (ITS) of ordered structures of LiMg_3 finds the ordered alloys to be intrinsically brittle. It is noted that alloying with certain elements may help to increase the intrinsic ductility.

II. COMPUTATIONAL APPROACH

The elastic constants, dislocation core structure relaxation, and phonon frequency were computed using VASP.^{23,24} Electron ion interactions were modeled using the projector augmented wave method. The Perdew, Becke, and Ernzerhof Generalized Gradient Approximation exchange-correlation functional was employed.²⁵ The Li valence states were chosen to be 1s2s2p while for Mg the 2p and 3s states were considered to be the valence states. Unless otherwise noted a plane-wave cutoff of 400 eV was used with a first order Methfessel-Paxton scheme employing a smearing parameter of 0.1 eV. Ionic relaxations were performed until the magnitudes of all residual forces were less than 5 meV/Å. The total energy was converged to within 10^{-6} eV/atom for all calculations except the elastic constants, in which case a convergence criterion of 10^{-8} eV/atom was used.

A. Dislocations

The dislocation core radius has no precise definition, but in effect describes the region near a dislocation in which continuum anisotropic linear elasticity theory (henceforth “linear elasticity theory”) is not valid. As no material can sustain a stress greater than its ISS, the regions for which linear elasticity theory predicts a stress state greater than the ISS are regions where linear elasticity theory is certainly incorrect. Accordingly, the dislocation core radius can be defined as the furthest distance from the center of a dislocation at which linear elasticity theory predicts the ISS.⁸ The dislocation core radius can then be estimated

with an approximation of the ISS in terms of the elastic constants and the Burgers vector of a dislocation using the Stroh formalism for a straight dislocation in an anisotropic medium.²⁶ In general, the core radius of a straight dislocation oriented in the $\langle uvw \rangle$ direction will change depending on the chosen shear plane, but in the case of the core radius for a $\langle 111 \rangle$ type screw dislocation in BCC the shear modulus oriented in this direction is isotropic with respect to shear plane allowing for the core radius to be written as

$$r_{core} = \frac{bK}{2\pi f G_{\langle 111 \rangle}}, \quad (1)$$

where b is the magnitude of the Burgers vector, K , the elastic modulus governing the dislocation line tension, $G_{\langle 111 \rangle}$, the shear modulus along the $\langle 111 \rangle$ direction (shear is isotropic along this direction in BCC), and f is a crystal structure dependent constant equal to approximately 0.11 in the case of BCC.^{27,28} K and $G_{\langle 111 \rangle}$ can be expressed as

$$K = \sqrt{(C_{11} - C_{12})C_{44}} \sqrt{\frac{2C_{11}^2 + 2C_{11}C_{12} - 4C_{12}^2 + 13C_{11}C_{44} - 7C_{12}C_{44} + 2C_{44}^2}{3(C_{11} - C_{12} + 4C_{44})(C_{11} + C_{12} + 2C_{44})}}, \quad (2)$$

$$G_{\langle 111 \rangle} = \frac{3C_{44}(C_{11} - C_{12})}{C_{11} - C_{12} + 4C_{44}}. \quad (3)$$

The ratio of $\frac{K}{G_{\langle 111 \rangle}}$ is a measure of elastic anisotropy. It should be noted that this differs from the Zener anisotropy, which is defined as $A = \frac{2C_{44}}{C_{11} - C_{12}}$, though both of these parameters show an increase in anisotropy with softening of C' .

The screw dislocation core radius is thus inversely proportional to the square root of the two shear moduli, C_{44} and C' . The softening of either shear modulus will result in the expansion of the dislocation core. Consequently, as a lattice instability is approached the dislocation core radius will expand. This makes binary Li-Mg especially interesting as its phase diagram shows only two stable phases (BCC and HCP) separated by a miscibility gap.¹³ In addition, the BCC phase is elastically unstable at ambient pressures suggesting that a lattice instability might be found as the concentration of magnesium is increased within a solid solution alloy.

The dislocation core near the BCC/HCP transition was analyzed at the atomic scale using a periodic supercell containing a $\langle 111 \rangle$ oriented screw dislocation dipole following the approach of Daw.²⁹ In this approach, elasticity theory is used to define the initial positions for

an atomic scale study of the dislocation cores. The distortion tensor of the periodic supercell is found by minimizing the elastic energy subject to the topological constraints imposed by the dislocations. The δ -function singularity in the dislocation density is approximated as a Gaussian distribution with a smearing of $b/5$. The distortion in the cell vectors due to the introduction of the dislocation quadrupole is determined as done by Lehto and Öberg.³⁰ The initial atomic displacements are then found by integrating the distortion tensor. These initial configurations are then relaxed using DFT in order to compute the dislocation core structures.

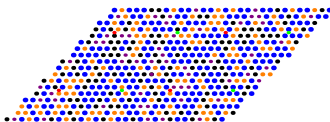


FIG. 1. Illustration of periodic dislocation quadrupole setup for a random alloy. The colors in the plot represent the two types of atoms at each site. The top layer is visible, the bottom layer is hidden by the first layer. Mg-Mg atomic columns are blue, Li-Li are purple, Li-Mg (top-bottom) are orange, and Mg-Li columns are black. The green dots correspond to the position of the singularity of the screw dislocations with a Burgers vector going into the page and the red dots represent the singularity positions of the screw dislocations with a Burgers vector coming out of the page.

For dislocation core structure calculations an initial cell consisting of 135 atoms was generated from elasticity theory. A 270 atom unit cell was then created by translating the unit cell by one lattice vector along $[111]$. The initial 270 atoms were then shuffled in order to create a disordered alloy at the desired composition (see FIG. 1). The cell was doubled along the line direction in order to better represent a random alloy. Ideally, the cell should be made thicker, but then the calculation becomes prohibitive. Atomic positions, but not the lattice vectors, were then relaxed using a $2 \times 1 \times 4$ Γ -centered grid. Analysis of the dislocation core structure was carried out using differential displacement maps as developed by Vitek *et al.*³¹ Compositional effects on the differential displacement map were minimized by relaxing two cells of identical arrangement of atom types, one cell with the dislocation quadrupole and the other with no dislocations. Displacements in the random alloy were subtracted from displacements in the quadrupole configuration to yield displacements due to the dislocations.

B. Elastic Constants

The elastic constants were calculated using a 16 atom special quasirandom structure (SQS) generated using the alloy theoretic automated toolkit.³² Both pairs and triplet clusters were considered within a range of $3a_0$, with a_0 being the lattice parameter of the crystal. Convergence tests were completed with respect to the number of k-points and varied depending on composition. However values were within the range of 1400 - 2000 points per reciprocal atom. The elastic constants were calculated by performing 4 deformations of varying magnitude for the six independent strains and after obtaining the stresses from VASP via the Hellmann-Feynmann theorem performing a linear fit.³³ As the SQS cell is not necessarily cubic the elastic tensor was symmetrized following the method of Tasnádi *et al.*³⁴

C. Phonons

As noted, the reduction in the value of C' is associated with the softening of acoustic phonon modes. However, the computational cost of an accurate calculation of the phonon dispersion of a binary solid solution such as Li-Mg using density functional theory (DFT) is prohibitive. This is due in part to the size of the unit cell needed to obtain a statistically representative distribution of atoms and the lack of any point symmetry in a random solution. However, an approximate phonon dispersion can be calculated using the Born-von Kármán constants.^{35,36} In this case only nearest- and next-nearest-neighbor contributions to the dynamical matrix are included, resulting in four parameters (α_1 , α_2 , β_2 , and γ_1) that can be determined from the elastic constants as well as the direct calculation of one phonon mode (in this case the H-phonon). The relation between the Born-von Kármán constants, elastic constants and H-phonon frequency can be written as³⁷

$$2(\alpha_1 + \alpha_2) = a_0 C_{11}, \quad (4a)$$

$$2(\alpha_1 + \beta_2) = a_0 C_{44}, \quad (4b)$$

$$4\gamma_1 = a_0(C_{12} + C_{44}), \quad (4c)$$

$$16\alpha_1 = M\omega_H^2, \quad (4d)$$

where a_0 is the lattice parameter, M is the atomic mass, and ω_H is the H-phonon frequency. For the relation between the dynamical matrix and the Born-von Kármán constants see the appendix (VII). The H-phonon frequency was calculated following the approach outlined by Ho *et al.*³⁸ The frequency was computed by determining the curvature of the energy according to equation 5 where $U_{\mathbf{q}}$ is the amplitude of the wave, $\Delta E_{\mathbf{q}}$ the change in energy per atom as a result of the phonon, and M is the average atomic mass of the system

$$\Delta E_{\mathbf{q}} = \frac{1}{2}M\omega_{\mathbf{q}}^2U_{\mathbf{q}}^2. \quad (5)$$

From the phonon dispersion not only can the dynamical stability of the material be determined, but the behavior of the $\Gamma \rightarrow N$ phonons can be considered. In BCC the N point corresponds to the $\langle \frac{1}{2}\frac{1}{2}0 \rangle$ direction in reciprocal space.³⁹ The softening of these phonons⁹ is associated with the transformation from BCC to HCP via the Burgers path¹⁰ and is an indication of proximity to the BCC/HCP transition.

The H-phonon frequency was calculated by generating four random, symmetrically inequivalent configurations of a 16 atom unit cell at the desired composition. The H-phonon displacements were then applied to each cell with the amplitude of displacement ranging from -1% to 1% of the lattice parameter. As these cells break cubic symmetry the phonon frequency along the [100], [010], and [001] directions was calculated and then averaged to obtain the H-phonon frequency. At each composition the averaged frequencies of all four configurations were within 2% of one another. Calculations were done using a $10 \times 10 \times 10$ Γ -centered K-point grid with a plane-wave cutoff energy of 500 eV.

D. Ideal Tensile Strength

For a material to be considered a viable candidate to plastically deform in bulk near its ideal strength it should be intrinsically ductile. Intrinsic ductility can be assessed by simulating a tensile load in a given direction and determining whether the crystal eventually reaches a shear instability or fails via cleavage. In the case of BCC materials it has been shown that the $\langle 100 \rangle$ directions are the weakest with respect to tensile loading.^{40,41} For an anisotropic material in a stressed state the elastic stability can be found using the condition

$$\lambda_{ijkl}\delta\epsilon_{ij}\delta\epsilon_{kl} \geq 0, \quad (6)$$

with λ_{ijkl} being the symmetric part of the Wallace tensor.^{42,43} Taking into account that λ_{ijkl} must be positive definite for elastic stability, in the case of tensile strain along [001] the following stability conditions must be maintained for a body centered tetragonal (BCT) structure.

$$(C_{33} + \sigma)(C_{11} + C_{22}) > (C_{13} - \frac{\sigma}{2})^2, \quad (7a)$$

$$C_{11} - C_{12} > 0, \quad (7b)$$

$$C_{66} > 0, \quad (7c)$$

$$C_{44} + \frac{\sigma}{2} > 0. \quad (7d)$$

Condition 7a corresponds to failure by cleavage while equations 7b-7d correspond to shear instabilities. Equation 7c is particularly important for the intrinsically ductile BCC transition metals (Ta, V, and Nb) as it represents the shear instability that initiates the orthorhombic path.⁴⁴ Using the FCT reference frame this corresponds to the shear stability condition $C_{11} - C_{12}$ introduced by Hill and Milstein.⁴⁵

ITS calculations were performed by applying a strain along [001] and relaxing the other lattice vectors such that all stresses, using the Hellman-Feynmann theorem, apart from σ_{33} were below 0.05 GPa. The elastic constants at each strain were then determined using a $21 \times 21 \times 21$ and $16 \times 16 \times 22$ Monkhorst-Pack grid in the case of the $D0_3$ and $L6_0$ ordered structures respectively.

III. RESULTS

In what follows, results for the three criteria for Gum-Metal-like behavior are described. The section begins with a presentation on the relationship between lattice softening and composition and its effects on the dislocation core and elastic anisotropy. This is followed by an analysis of the effect of composition on the softening of the acoustic phonon modes associated with the Burgers transformation path, and ends with an assessment of LiMg ordered structures' intrinsic ductility.

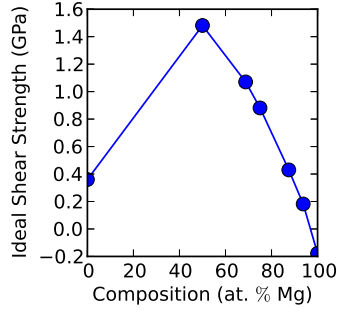
A. Elasticity Theory

FIG. 2 shows several noticeable trends in ISS, elastic moduli, as well as core radius of an $\langle 111 \rangle$ type screw dislocation. Li-Mg alloys appear to show a high ratio of the Young's modulus to shear modulus along $\langle 111 \rangle$, which is consistent with how Ti-V is found to behave.⁷ As FIG. 2c illustrates, this behavior can be tied to the anisotropy parameter $K/G_{\langle 111 \rangle}$. The anisotropy parameter is also directly proportional to the dimensionless pinning length, l_c^* .⁷ This parameter determines the average obstacle spacing necessary for a dislocation to be pinned.

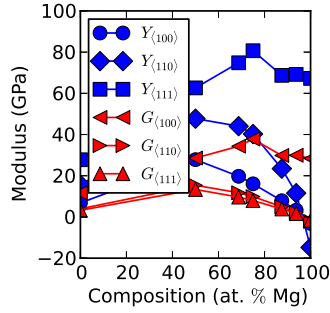
The ISS estimated from the elastic constants ($0.11G_{\langle 111 \rangle}$) appears to decrease with an increase in anisotropy. The ISS can be estimated as approximately 0.8 - 1.0 GPa at the experimental BCC/HCP transition (approximately 71 at. % Mg).¹³ The resulting core radius predicted from elasticity theory is abnormally large. For reference the core radius of tungsten is approximately $1.45b$ while that of a known Gum Metal, Ti36Nb2Ta3Zr0.30 (wt.%), is $1.51b$.⁴⁶ It is important to note that although the core radius of a $\langle 111 \rangle$ screw dislocation in Gum Metal does not appear to be that different than that of tungsten, because of the fact that Gum Metal exists near an elastic instability, composition fluctuations can lead to large dislocation core regions. This is illustrated in FIG. 2c, where the elastic anisotropy as well as the core radius increase rapidly near the elastic instability.

B. Dislocation Core Structure

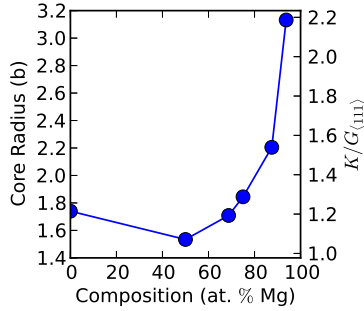
The dislocation core structure as calculated from DFT at 68.75 at. % Mg of a quadrupole configuration for $\langle 111 \rangle$ type screw dislocations as shown in FIG. 3 displays a large degree of core spreading on the (111) plane in agreement with the results from elasticity theory. This particular composition was chosen as it is near to the experimental BCC/HCP phase transition at room temperature. Of particular interest are the large lateral displacements of atomic columns shown in FIG. 3b. The displacements become so large in areas that localized shearing of the crystal appears to have occurred. The structure is reminiscent of the nanodisturbances detected in Gum Metal.²² The localized shearing occurs in the region between dislocation cores highlighted in FIG. 3a. This same behavior has been identified in other investigations of Ti-V⁸ and BCC Mg at high pressure.⁴⁷ It appears to suggest that the



a)



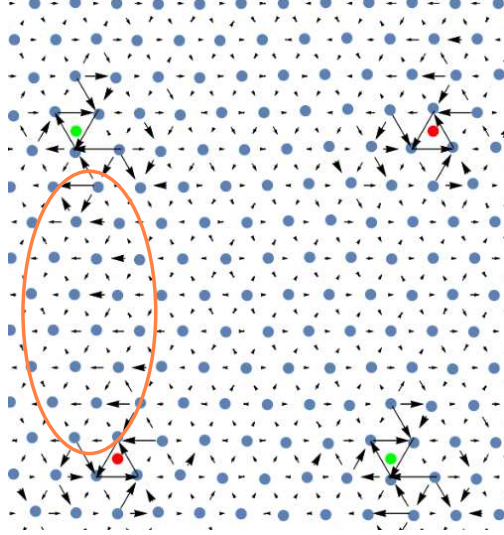
b)



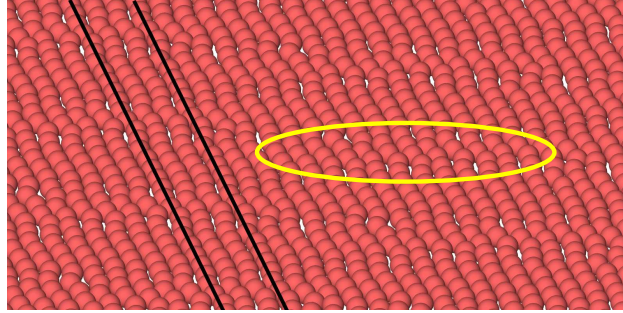
c)

FIG. 2. The ISS is estimated from the elastic constants of Li-Mg at various compositions (2a). A reduction in the ISS corresponds to a high degree of anisotropy between the Young's modulus and shear modulus along different axes (2b). A measure for the anisotropy of the crystal $K/G_{\langle 111 \rangle}$ is shown to have a significant affect on the core radius (2c). The core radius at all compositions studied is higher than that predicted for Gum Metal.

formation of these nanodisturbance-like structures is a result of dislocation core interaction, possibly due to the overlap of spread dislocation cores.



a)



b)

FIG. 3. The dislocation core (3a) shows a large degree of spreading. Along the vertical axis the region between dislocations appears to show large displacements (orange oval). The projection of atomic columns in a quadrupolar dislocation configuration onto the (111) plane is shown in 3b. All displacements due to compositional effects have been removed from the projections, meaning displacements shown are a result of dislocation interactions. Large lateral displacements are seen in the projection. For reference two straight black lines are drawn. Lateral shifts are especially large in the area within the yellow oval.

C. Lattice Dynamics

As the HCP phase is approached (Mg content is increased) FIG. 4 shows the softening of the $\Gamma \rightarrow N$ branch. Specifically it can be shown that the lattice shuffling resulting from the N-phonon coupled with a near $\langle 1\bar{1}2 \rangle \{111\}$ (approximately 13° from $\langle 1\bar{1}2 \rangle$ on a $\{111\}$ plane) shear transforms the BCC phase to HCP.⁹ The orientation of the shear associated with this

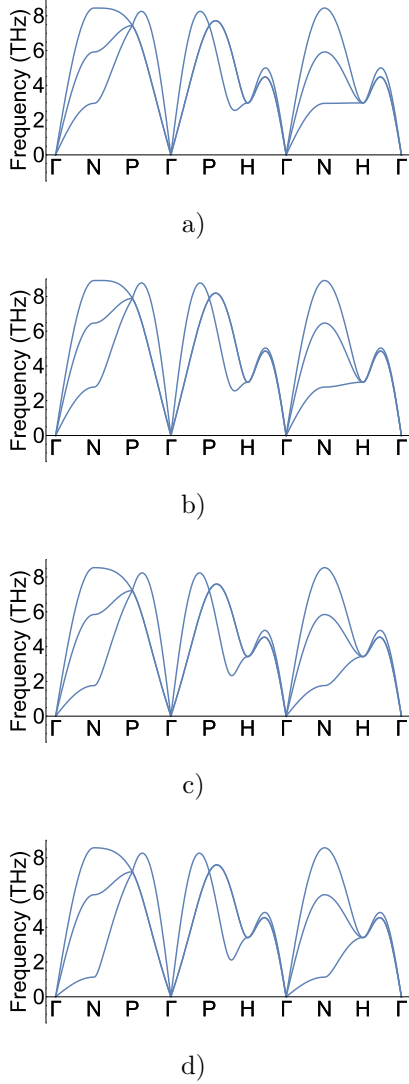


FIG. 4. The phonon dispersion is plotted for increasing compositions of Mg from 68.75 at. % (4a) 75 at. % (4b) 87.5 at. % (4c) and 93.75 at. % (4d). The formation of soft phonons along $\Gamma \rightarrow N$ can clearly be seen with increasing magnesium content.

transformation is approximately the same as the large shear faults that have been reported in Gum Metal.¹ In addition, the N-phonon appears lower than the phonon associated with the transformation of BCC to the hexagonal ω phase,³⁷ which corresponds to the lowest frequency between the P and H points in the dispersion ($\mathbf{q}_\omega \approx (\frac{1}{3}, \frac{1}{3}, \frac{2}{3})$). It seems then unlikely from these observations that a transformation path other than the Burgers path would be preferred.

D. Ideal Tensile Behavior

For a material to be a possible candidate for Gum Metal it should be intrinsically ductile.⁷ ITS calculations were carried out on two BCC-type ordered structures near the BCC/HCP transition (D0₃ and L6₀) to approximate the behavior of a Li-Mg alloy at 75 at. % Mg. These two structures were used to approximate a random alloy at this composition. The D0₃ structure can be defined in terms of a primitive unit cell of the face-centered cubic lattice with four atoms of the form

$$\mathbf{a} = \frac{a_0}{2}(\mathbf{e}_2 + \mathbf{e}_3), \quad (8a)$$

$$\mathbf{b} = \frac{a_0}{2}(\mathbf{e}_1 + \mathbf{e}_3), \quad (8b)$$

$$\mathbf{c} = \frac{a_0}{2}(\mathbf{e}_1 + \mathbf{e}_2), \quad (8c)$$

$$\boldsymbol{\tau}_1^{Li} = \mathbf{0}, \quad (8d)$$

$$\boldsymbol{\tau}_2^{Mg} = \frac{1}{4}\mathbf{a} + \frac{1}{4}\mathbf{b} + \frac{1}{4}\mathbf{c}, \quad (8e)$$

$$\boldsymbol{\tau}_3^{Mg} = \frac{1}{2}\mathbf{a} + \frac{1}{2}\mathbf{b} + \frac{1}{2}\mathbf{c}, \quad (8f)$$

$$\boldsymbol{\tau}_4^{Mg} = \frac{3}{4}\mathbf{a} + \frac{3}{4}\mathbf{b} + \frac{3}{4}\mathbf{c}. \quad (8g)$$

L6₀ is related to the L1₂ structure as BCC is related to FCC along the Bain path. According to FIG. 5 both the D0₃ and L6₀ structures are intrinsically brittle, with the two structures displaying cleavage failure at approximately 9% and 8% strain respectively.

In addition, the energy- and stress-strain curves for the two ordered structures are displayed in FIGs. 6 and 7. In the case of L6₀ failure in cleavage is in keeping with the behavior of the energy and stress curves for the tetragonal path, which show the stabilization of FCC at approximately 25 – 30% strain (see FIG. 7). The material is preferentially following the Bain transformation path. Since FCC is shown from the energy curve to be metastable, a maximum stress must exist between the FCC and BCC phases, meaning that the material fails via cleavage; it is intrinsically brittle. This is in agreement with the estimate of the Pugh ratio.¹⁸

Viewing FIGs. 6b and 7b it should be noted that the stress-strain curves obtained directly from VASP using the Hellmann-Feynman theorem are not smooth. The scattering of the stress values is likely a result of the low strength of the two ordered Li-Mg structures

considered in this work, meaning cutoff stresses used in the minimization routine for the ideal strength lower than 0.05 GPa would likely be needed to smoothen the curve further. In order to gain a better understanding of the error in the stress calculations, stress was also estimated directly from the energy-strain curves shown in FIGs. 6a and 7a. The stress was estimated by fitting the energy-strain curves to a third degree spline function and then taking the derivative of energy per unit volume with respect to strain. The difference in stress between the two approaches was calculated to be 0.1 GPa on average for both structures considered with maximum differences in stress being approximately 0.2 GPa for both structures. While this difference is sizable compared to the ITS of the D0₃ and L6₀ structures, both approaches show the local maximum and minimum stresses appearing at approximately the same strains.



FIG. 5. The elastic stability criteria plotted as a function of strain for the D0₃ and L6₀ structures at a composition of 75 at. % Mg (FIGs. 5a and 5b respectively). The plot shows that a failure via cleavage occurs at a strain of approximately 9% for the D0₃ structure and a strain of 8% for L6₀.



FIG. 6. The stress-strain and energy-strain relation for the $D0_3$ structure under a $\langle 100 \rangle$ type tensile load. Only the tetragonal path is explored in this simulation. In FIG. 6b “Hellmann-Feynman” refers to the stresses obtained directly from VASP using the Hellman-Feynman theorem and “Fitted from Energy” refers to the stresses obtained by taking the derivative of energy per unit volume with respect to strain.



FIG. 7. The stress-strain and energy-strain relation for the $L6_0$ structure under a $\langle 100 \rangle$ type tensile load. Only the tetragonal path is explored in this simulation. The formation of the FCC phase can be seen at a strain of approximately 25 – 30%. This corresponds to the ordered $L1_2$ structure. In FIG. 7b “Hellmann-Feynman” refers to the stresses obtained directly from VASP using the Hellman-Feynman theorem and “Fitted from Energy” refers to the stresses obtained by taking the derivative of energy per unit volume with respect to strain.

IV. DISCUSSION

From the first-principles ITS calculations it is not clear if the compositions of Li-Mg studied so far will behave as Gum Metal. This is due to the intrinsically brittle behavior seen for the ordered phases. Interestingly, Li *et al.* found this to be the case for TiV alloys using the virtual crystal approximation⁷ even at the special number of 4.24 valence electrons per atom. An initial guess at the origin of the brittle behavior comes from viewing the elastic constants. Due to symmetry, BCC crystals’ ideal shear and tensile strengths can be approximated from their elastic constants ($\sigma_{ISS} \approx 0.11G_{\langle 111 \rangle}$ and $\sigma_{ITS} \approx 0.08Y_{\langle 100 \rangle}$),^{27,28}

assuming that no shear instability takes place along the deformation path. By viewing intrinsic ductility as a competition between these two strengths, one should then be able to estimate the intrinsic ductility of a crystal by examining the ratio $\frac{G_{\langle 111 \rangle}}{Y_{\langle 100 \rangle}}$. With this in mind, Table I shows $\frac{G_{\langle 111 \rangle}}{Y_{\langle 100 \rangle}}$ to be near 0.5 for all considered compositions of Li-Mg. This is not only higher than the intrinsically ductile Nb and V whose values are approximately 0.15-0.25, but other intrinsically brittle BCC metals such as Mo and W with ratios of roughly 0.35 - 0.40.⁴⁴ However, this analysis appears to only work for BCC materials that see an elastic instability as a result of $C_{66} \rightarrow 0$ for a $\langle 100 \rangle$ tensile load. For instance, a Ti₃Nb Gum Metal approximant is calculated to have $\frac{G_{\langle 111 \rangle}}{Y_{\langle 100 \rangle}} = 0.42$ and the crystal is predicted to be intrinsically ductile as a result of $C' \rightarrow 0$.⁴⁸ Looking at the ratio of moduli in terms of the cubic elastic constants, which is written as

TABLE I. Elastic constants of Li-Mg alloys as a function of composition. The elastic constants are written in units of GPa.

Composition [at. % Mg]	C_{11}	C_{12}	C_{44}	$\frac{G_{\langle 111 \rangle}}{Y_{\langle 100 \rangle}}$
0	17.9	13.2	11.7	0.478
50	39.9	18.8	28.6	0.479
68.75	39.8	25.7	34.3	0.488
75	38.7	27.3	37.8	0.493
87.5	36.5	31.1	29.8	0.491
93.75	35.0	32.8	29.9	0.496
100	34.0	36.1	28.4	0.504

$$\frac{G_{\langle 111 \rangle}}{Y_{\langle 100 \rangle}} = \frac{3(C_{11} + C_{12})C_{44}}{(C_{11} + 2C_{12})(C_{11} - C_{12} + 4C_{44})}, \quad (9)$$

shows that for $C_{11} = C_{12}$ the ratio becomes exactly $\frac{1}{2}$. While C' is soft, as FIG. 5 shows, with the application of a uniaxial stress C' actually increases until failure occurs. This suggests the importance of higher-order elastic constants in determining the failure mode of the material.^{49,50}

For the orthorhombic path to be activated in Li-Mg alloys (for intrinsic ductility to be obtained), the shear instability that initiates the orthorhombic path must be designed to

occur before cleavage can occur. Within the FCO reference frame the condition $C_{11} - C_{12} < 0$ must occur sooner in the tensile load. The tensile loading of a BCC crystal can result in two possible sequences of stress-free states. The BCC→FCC→BCT ordering is consistent with the tensile path while the BCC→BCT→FCC corresponds to an orthorhombic path.^{44,51} It follows that if the FCC phase could be made elastically unstable then the orthorhombic path would be preferred, and intrinsic ductility could be achieved. This approach, however, is not perfect, as illustrated by ITS calculations of the DO_3 structure (FIG. 6), in which case the FCC phase is not associated with a local energy minimum yet the BCC phase is still found to be intrinsically brittle. Another possible approach involves alloying Li-Mg alloys with the elements that were previously found to increase the Pugh ratio for an ordered Li-Mg compound: Mn, Fe, Co, Ni, Cl, and Cu.²¹ It is also possible that Li-Mg alloys undergo a brittle-ductile transition at some point below room temperature, which would negate the need to perform any alloying in order to achieve intrinsic ductility.

If Li-Mg alloys can be tuned to be intrinsically ductile, then they become an intriguing structural alloy. Assuming that yield stresses near 40 – 50% of the ISS could be reached, at a composition of 68.75 at. % Mg a specific strength of roughly 290-440 MPa cm³ g⁻¹ would be possible. In comparison, the specific strength of Gum Metal is approximately 194 MPa cm³ g⁻¹,¹ while high-specific-strength steels (HSSS⁵²) have been able to achieve specific strengths of approximately 190 MPa cm³ g⁻¹.

V. CONCLUSION

A first-principles investigation of the mechanical properties of a range of Li-Mg alloys is presented. Analysis of the elastic constants of solid solutions using special quasirandom structures shows many similarities in the behavior of the elastic constants of Li-Mg with those of Gum Metal as the BCC/HCP transition composition is approached. A large elastic anisotropy due to the softening of the modulus C' results in a large nondimensional dislocation pinning length as well as large dislocation core radii. Associated with this behavior is the emergence of large shear faults in the dislocation cores. As the material is found to be intrinsically brittle at all compositions studied more work is needed to make the structure intrinsically ductile.

VI. ACKNOWLEDGMENTS

The authors acknowledge insightful discussions with Prof. Mark Asta. I.S.W. and D.C.C. acknowledge funding through the Materials Project Center funded by the Department of Energy Basic Energy Science grant No. EDCBEE. T.T. recognizes financial support from the Japan Society for the Promotion of Science (JSPS), Grant-in-Aid for Scientific Research (No. 16K06714).

VII. APPENDIX

For a given reciprocal vector, $\mathbf{q} = \frac{2\pi}{a_0}(p_1, p_2, p_3)$, the dynamical matrix can be defined as follows

$$\Phi_{11}(\mathbf{q}) = 8\alpha_1[1 - \cos(\pi p_1) \cos(\pi p_2) \cos(\pi p_3)] + 2\alpha_2[1 - \cos(2\pi p_1)] + 2\beta_2[2 - \cos(2\pi p_2) - \cos(2\pi p_3)], \quad (10a)$$

$$\Phi_{22}(\mathbf{q}) = 8\alpha_1[1 - \cos(\pi p_2) \cos(\pi p_3) \cos(\pi p_1)] + 2\alpha_2[1 - \cos(2\pi p_2)] + 2\beta_2[2 - \cos(2\pi p_3) - \cos(2\pi p_1)], \quad (10b)$$

$$\Phi_{33}(\mathbf{q}) = 8\alpha_1[1 - \cos(\pi p_3) \cos(\pi p_1) \cos(\pi p_2)] + 2\alpha_2[1 - \cos(2\pi p_3)] + 2\beta_2[2 - \cos(2\pi p_1) - \cos(2\pi p_2)], \quad (10c)$$

$$\Phi_{12}(\mathbf{q}) = 8\gamma_1 \sin(\pi p_1) \sin(\pi p_2) \sin(\pi p_3), \quad (10d)$$

$$\Phi_{23}(\mathbf{q}) = 8\gamma_1 \sin(\pi p_2) \sin(\pi p_3) \sin(\pi p_1), \quad (10e)$$

$$\Phi_{13}(\mathbf{q}) = 8\gamma_1 \sin(\pi p_3) \sin(\pi p_1) \sin(\pi p_2). \quad (10f)$$

* ian.winter@berkeley.edu

† dcchrzan@berkeley.edu

¹ T. Saito, T. Furuta, J.-H. Hwang, S. Kuramoto, K. Nishino, N. Suzuki, R. Chen, A. Yamada, K. Ito, Y. Seno, T. Nonaka, H. Ikehata, N. Nagasako, C. Iwamoto, Y. Ikuhara, and T. Sakuma, *Science* **300**, 464 (2003).

² H. Xing, J. Sun, Q. Yao, W. Guo, and R. Chen, *Applied Physics Letters* **92**, 151905 (2008).

- ³ P. Castany, M. Besse, and T. Gloriant, [Phys. Rev. B **84**, 020201 \(2011\)](#).
- ⁴ R. Talling, R. Dashwood, M. Jackson, and D. Dye, *Acta Materialia* **57**, 1188 (2009).
- ⁵ H. Kim, Y. Ikehara, J. Kim, H. Hosoda, and S. Miyazaki, *Acta Materialia* **54**, 2419 (2006).
- ⁶ J.-P. Liu, Y.-D. Wang, Y.-L. Hao, Y. Wang, Z.-H. Nie, D. Wang, Y. Ren, Z.-P. Lu, J. Wang, H. Wang, *et al.*, *Scientific reports* **3**, 2156 (2013).
- ⁷ T. Li, J. W. Morris, N. Nagasako, S. Kuramoto, and D. C. Chrzan, [Phys. Rev. Lett. **98**, 105503 \(2007\)](#).
- ⁸ D. C. Chrzan, M. P. Sherburne, Y. Hanlumuayang, T. Li, and J. W. Morris, [Phys. Rev. B **82**, 184202 \(2010\)](#).
- ⁹ Y. Hanlumuayang, R. P. Sankaran, M. P. Sherburne, J. W. Morris, and D. C. Chrzan, [Phys. Rev. B **85**, 144108 \(2012\)](#).
- ¹⁰ W. Burgers, [Physica **1**, 561 \(1934\)](#).
- ¹¹ I. S. Winter, M. de Jong, M. Asta, and D. C. Chrzan, (submitted for publication) (2017).
- ¹² G. V. Sin'ko and N. A. Smirnov, [Phys. Rev. B **80**, 104113 \(2009\)](#).
- ¹³ A. Hashemi, A. Pelton, and J. B. Clark, *Binary Alloy Phase Diagrams* **3**, 2444 (1990).
- ¹⁴ M. Furui, H. Kitamura, H. Anada, and T. G. Langdon, *Acta Materialia* **55**, 1083 (2007).
- ¹⁵ M. Furui, C. Xu, T. Aida, M. Inoue, H. Anada, and T. G. Langdon, *Materials Science and Engineering: A* **410**, 439 (2005).
- ¹⁶ H. Matsunoshita, K. Edalati, M. Furui, and Z. Horita, *Materials Science and Engineering: A* **640**, 443 (2015).
- ¹⁷ S. Kuramoto, T. Furuta, N. Nagasako, and Z. Horita, [Appl. Phys. Lett. **95**, 1 \(2009\)](#).
- ¹⁸ W. Counts, M. Friák, D. Raabe, and J. Neugebauer, *Acta Materialia* **57**, 69 (2009).
- ¹⁹ I. Shin and E. A. Carter, *Acta Materialia* **64**, 198 (2014).
- ²⁰ S. Pugh, *The London, Edinburgh, and Dublin Philosophical Magazine and Journal of Science* **45**, 823 (1954).
- ²¹ W. A. Counts, M. Friak, D. Raabe, and J. Neugebauer, *Advanced Engineering Materials* **12**, 1198 (2010).
- ²² M. Y. Gutkin, T. Ishizaki, S. Kuramoto, and I. A. Ovid'ko, [Acta Mater. **54**, 2489 \(2006\)](#).
- ²³ G. Kresse and J. Furthmüller, [Phys. Rev. B **54**, 11169 \(1996\)](#).
- ²⁴ G. Kresse and J. Hafner, [Phys. Rev. B **47**, 558 \(1993\)](#).
- ²⁵ J. P. Perdew, K. Burke, and M. Ernzerhof, [Phys. Rev. Lett. **77**, 3865 \(1996\)](#).

- ²⁶ A. N. Stroh, *Philos. Mag.* **3**, 625 (1958).
- ²⁷ C. R. Krenn, D. Roundy, J. W. Morris, and M. L. Cohen, *Mater. Sci. Eng. A* **319**, 111 (2001).
- ²⁸ D. Roundy, C. R. Krenn, M. L. Cohen, and J. W. Morris, *Philos. Mag. A* **81**, 1725 (2001).
- ²⁹ M. S. Daw, *Computational Materials Science* **38**, 293 (2006).
- ³⁰ N. Lehto and S. Öberg, *Phys. Rev. Lett.* **80**, 5568 (1998).
- ³¹ V. Vitek, R. C. Perrin, and D. K. Bowen, *Philosophical Magazine* **21**, 1049 (1970).
- ³² A. van de Walle, P. Tiwary, M. de Jong, D. Olmsted, M. Asta, A. Dick, D. Shin, Y. Wang, L.-Q. Chen, and Z.-K. Liu, *Calphad* **42**, 13 (2013).
- ³³ M. de Jong, D. L. Olmsted, A. van de Walle, and M. Asta, *Phys. Rev. B* **86**, 224101 (2012).
- ³⁴ F. Tasnádi, M. Odén, and I. A. Abrikosov, *Phys. Rev. B* **85**, 144112 (2012).
- ³⁵ H. Cook and D. De Fontaine, *Acta Metallurgica* **17**, 915 (1969).
- ³⁶ C. B. Walker, *Phys. Rev.* **103**, 547 (1956).
- ³⁷ D. De Fontaine, *Acta metallurgica* **18**, 275 (1970).
- ³⁸ K.-M. Ho, C. L. Fu, and B. N. Harmon, *Phys. Rev. B* **29**, 1575 (1984).
- ³⁹ M. Lax, *Symmetry principles in solid state and molecular physics* (John Wiley and Sons, 1974).
- ⁴⁰ F. Milstein and S. Chantasiriwan, *Phys. Rev. B* **58**, 6006 (1998).
- ⁴¹ M. Šob, L. Wang, and V. Vitek, *Materials Science and Engineering: A* **234**, 1075 (1997).
- ⁴² D. C. Wallace, *Thermodynamics of Crystals* (Courier Corporation, 1998).
- ⁴³ W. Morris Jr and C. R. Krenn, *Philos. Mag. A* **80**, 2827 (2000).
- ⁴⁴ N. Nagasako, M. Jahnátek, R. Asahi, and J. Hafner, *Phys. Rev. B* **81**, 94108 (2010).
- ⁴⁵ R. Hill and F. Milstein, *Phys. Rev. B* **15**, 3087 (1977).
- ⁴⁶ R. Talling, R. Dashwood, M. Jackson, and D. Dye, *Scripta Materialia* **60**, 1000 (2009).
- ⁴⁷ I. S. Winter, M. Poschmann, T. Tsuru, and D. C. Chrzan, *Phys. Rev. B* **95**, 064107 (2017).
- ⁴⁸ N. Nagasako, R. Asahi, and J. Hafner, *Phys. Rev. B* **85**, 024122 (2012).
- ⁴⁹ M. de Jong, I. S. Winter, D. C. Chrzan, and M. Asta, *Phys. Rev. B* (accepted) (2017).
- ⁵⁰ H. Wang and M. Li, *Phys. Rev. B* **85**, 104103 (2012).
- ⁵¹ F. Milstein, J. Marschall, and H. E. Fang, *Phys. Rev. Lett.* **74**, 2977 (1995).
- ⁵² S.-H. Kim, H. Kim, and N. J. Kim, *Nature* **518**, 77 (2015).